

SCIENTIFIC REPORTS

OPEN

Rectifying the output of vibrational piezoelectric energy harvester using quantum dots

Lijie Li

Received: 21 December 2016

Accepted: 20 February 2017

Published: 20 March 2017

Piezoelectric energy harvester scavenges mechanical vibrations and generates electricity. Researchers have strived to optimize the electromechanical structures and to design necessary external power management circuits, aiming to deliver high power and rectified outputs ready for serving as batteries. Complex deformation of the mechanical structure results in charges with opposite polarities appearing on same surface, leading to current loss in the attached metal electrode. External power management circuits such as rectifiers comprise diodes that consume power and have undesirable forward bias. To address the above issues, we devise a novel integrated piezoelectric energy harvesting device that is structured by stacking a layer of quantum dots (QDs) and a layer of piezoelectric material. We find that the QD can rectify electrical charges generated from the piezoelectric material because of its adaptable conductance to the electrochemical potentials of both sides of the QDs layer, so that electrical current causing energy loss on the same surface of the piezoelectric material can be minimized. The QDs layer has the potential to replace external rectification circuits providing a much more compact and less power-consumption solution.

Piezoelectric effect is exhibited in crystals with no centre of symmetry. Under an external stress, a net polarization appears on the surface of the material, generating piezoelectric voltage, inducing electrical charges. Mechanical-to-electrical energy harvesting devices based on piezoelectric materials have been receiving much attention in recent decades^{1–4}. Moreover it has been successfully advanced to nanoscale energy devices recently^{5,6}. Note that charge can only be continuously generated when there is a change in the applied force, which means that a static force only generates a fixed amount charges that will leak away quickly across the external circuit (internal screening effect is neglected). The time taken for leaking away all generated charges depends on the input impedance of the external circuit. For instance a $1\text{ k}\Omega$ load resistance R_L and a 1 nF internal capacitance C_p of the piezoelectric transducer results in a time constant of $R_L \times C_p = 1\text{ }\mu\text{s}$, which implies that after $1\text{ }\mu\text{s}$ all generated charges from a static mechanical force disappear. For this reason the device works mainly under AC conditions for energy harvesting purpose, in order to continuously generate electrical charges. This brought out the concept of ‘vibrational’ energy harvesting structures.

The optimal power generation is when the device operates at its resonant frequency⁷, which leads to essential additions of external rectifying circuits^{8–10}, causing unavoidable power consumptions. The vibrational energy harvesters usually appear in the form of a cantilever with one end fixed, the other suspended^{11–14}, as mechanical cantilevers are able to generate larger strain, easy to fabricate, and having lower fundamental frequencies to match with ambient mechanical sources. Although tremendous efforts have been spent to increase the output power of the cantilever harvester, including some innovative structural designs^{15–17}. There is an ongoing issue of designing low power consumption AC-DC converters for rectifying the AC output of the harvester^{18–20}. Complex vibrations of the cantilever subjecting to arbitrary excitations from ambient sources sometimes result in both positive and negative charges accumulating on the same surface, subsequently introducing electrical current on the metal electrode attaching to that piezoelectric surface. This amount of power loss is not compensatable using the external circuits. We used segmentation protocol aiming for collecting positive and negative charges separately^{21–23}, essentially creating many sub-cells. However it will require more complex external circuits to handle these sub-cells, and the consequence will be more electrical power dissipated in the power management circuits.

Inspired from the electron quantum transport theory of conductors²⁴, we propose to coat a layer of QDs onto the piezoelectric cantilever (schematic diagram is shown in Fig. 1a). The QD layer is able to function as

Multidisciplinary Nanotechnology Centre, College of Engineering, Swansea University, Bay Campus, Swansea, SA1 8EN, UK. Correspondence and requests for materials should be addressed to L.L. (email: L.Li@swansea.ac.uk)

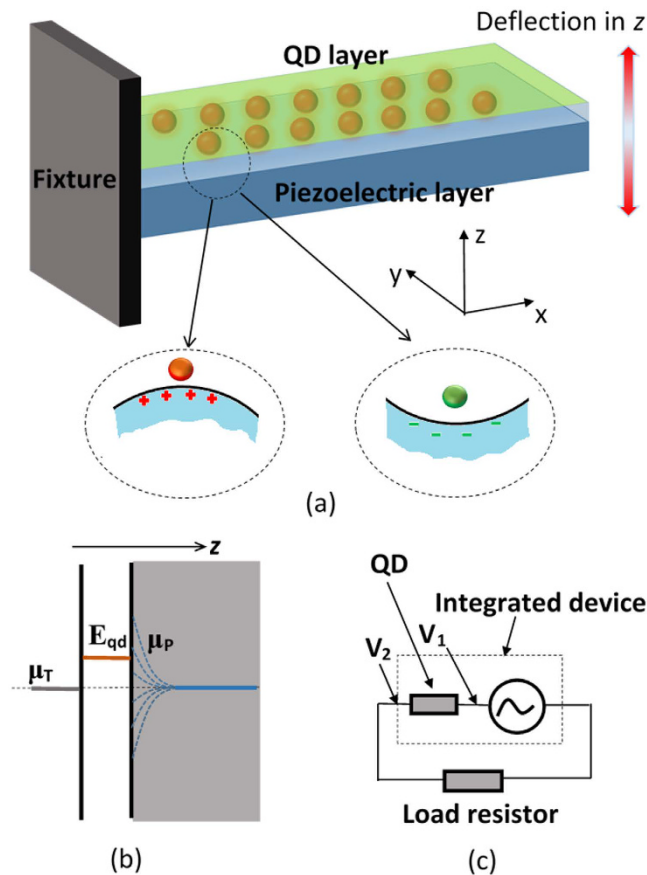


Figure 1. Schematic view of the integrated energy harvester. (a) 3D view of the stacked QD and piezoelectric layers. Circled diagrams show the principle of adaptable conductance of the QD subjecting to different surface charges, where red dot represents low conductance, green dot shows high conductance. (b) Energy diagram of the electrode-QD-piezoelectric interface. (c) equivalent circuit of the device.

an integrated filter or rectifier that has adaptable resistance under different chemical potentials of both sides of the QDs layer, which are the metal electrode and piezoelectric material respectively. Thus charges with different polarities and quantities cause variation of electrochemical potential of the piezoelectric surface attaching to the QDs layer, adjusting the resistance of the QDs layer. The theory and method underpinning this hypothesis is detailed in the next section, followed by the numerical case study. This new method is much more efficient than previous approaches of using external circuits or segmenting electrodes, since it does not need additional circuits consisting of active electronic components like transistors, diodes. This design seamlessly integrates power management circuits with the actual transducer, moreover it significantly reduces power loss on the same surface of the piezoelectric material in the cases of the harvester experiencing complex deformations.

Models and Methods

The multiphysical treatment for this new concept is split into three steps, namely mechanical-to-electrical (MTE), charge-to-electrochemical potential (CTE), and elastic tunnelling (ET) through the quantum dot. Euler-Bernoulli beam theory together with the constitutive piezoelectric equation will be used in the MTE stage, CTE simulation is based on semiconductor physics, and ET simulation is built on the quantum mechanics theory. This open-loop multi-physics simulation links the external applied mechanical excitation to the conductance of the QD, through which the rectifying function of this concept is demonstrated. Finally this integrated device is connected to a load resistor for demonstration in the real applications.

Mechanical strain to electrical charge. To begin with the analysis, we describe the integrated energy harvester as the form of a cantilever, which consists of a layer of piezoelectric material acting as the strain to electrical charge converter, and a layer of quantum dots that can be spin coated or printed. In the real scenario, metal electrodes are plated on both sides of the composite cantilever. Due to very thin electrode layer, its mechanical contribution is neglected in the analysis. The length L , width w , and thickness g of the piezoelectric layer are designated as 5 mm , 0.5 mm , and $50\text{ }\mu\text{m}$ for the later numerical demonstration. AlN is chosen as the piezoelectric material with density ρ of 3300 kg/m^3 ²⁵, Poisson's ratio ν and Young's modulus Y of 350 GPa ²⁶. The quantum dots layer is so thin (normally $<1\text{ }\mu\text{m}$), and it can also be neglected in the mechanical analysis. The dynamic motion of the cantilever can be described using the mass-spring-damper equation²⁷

$$m_t \ddot{z} + b \dot{z} + k_1 z + k_2 z^3 = A \cos(\omega t) \quad (1)$$

where m_t , b , k_1 , k_2 are total effective mass ($\frac{33}{140} + 100$) $Lwg\rho$ (here we attach an additional proof mass ($100 \times Lwg\rho$) at the free end of the cantilever to reduce the resonant frequency), damping coefficient, linear stiffness, and non-linear stiffness respectively. $z(t)$ is the tip displacement. The first derivative of the z with respect to the time t represents the velocity, and the second derivative denotes the acceleration. A is the amplitude of the external periodic driving force, and ω is the driving frequency. When $\omega = \omega_0$ (ω_0 being the natural frequency of the cantilever $\omega_0 = \sqrt{\frac{k_1}{m_t}}$, here we only analyse the fundamental resonance), the deformation of the cantilever reaches to the maximum. Here we set the driving frequency same as the nature frequency of the cantilever to ensure an optimal match between the excitation and the beam. Under the external driving, the cantilever vibrates, the deflected cantilever can be treated as an arc. The curvature $1/r$ (r is the radius) of this arc is expressed with respect to the tip deflection z

$$\frac{1}{r(t)} = \frac{2z(t)}{L^2} \quad (2)$$

The axial strain on the surface of the piezoelectric layer along the x -axis can be obtained in terms of curvature and tip deflection²⁷

$$\varepsilon_x(t) = \frac{g}{2r(t)} \quad (3)$$

The axial stress σ in the piezoelectric layer is derived through the stress-strain relation, that is $\sigma_x(t) = Y\varepsilon_x(t)$. The piezoelectric constitutive equations relate four field variables stress components Σ , strain components S , electric field components E , and the electric displacement components D , which can be described as $\begin{bmatrix} S \\ D \end{bmatrix} = \begin{bmatrix} s^E & d^t \\ d & \varepsilon^T \end{bmatrix} \begin{bmatrix} \Sigma \\ E \end{bmatrix}$ ^{28,29}. We shall focus on the generated electric displacement D from the mechanical stress Σ . Assuming no external electric field is applied to the cantilever, $D = d\Sigma$, d being the piezoelectric constant. The electrical charges generated from a tip deflection $z(t)$ can therefore be obtained

$$Q(t) = wLd_{31}\sigma_x(t) = \frac{wd_{31}Yg}{L}z(t) \quad (4)$$

where d_{31} is the piezoelectric constant, relating the strain in the '1' direction (x -direction) to a generated field along the '3' direction (z -direction). In the simulation, we take $d_{31} = -1.9$ pC/N³⁰. A upward deflection ($z > 0$) corresponds to a compressive stress on the top surface, therefore inducing negative charges.

Charge to electrochemical potential. After obtaining piezoelectrically generated charges, electrochemical potentials (top and bottom surface) of the piezoelectric layer can be derived from the carrier density equation³¹, which is

$$\begin{aligned} n &= \int_0^\infty D_3(\mathcal{E})f_0(\mathcal{E})d\mathcal{E} \\ &= \frac{1}{2\pi^2} \left(\frac{2m^*}{\hbar^2} \right)^{3/2} \int_0^\infty \frac{\mathcal{E}^{1/2}}{\exp\left(\frac{\mathcal{E}-\mu}{k_B T}\right) + 1} d\mathcal{E} \end{aligned} \quad (5)$$

where $D_3(\mathcal{E})$ is the density of state for 3-dimensional bulk materials, which takes the form of $\frac{1}{2\pi^2} \left(\frac{2m^*}{\hbar^2} \right)^{3/2} \mathcal{E}^{1/2}$ ³², where \hbar is the reduced Planck's constant (1.05×10^{-34} Js), m^* is the effective mass of electron $m^* = 0.33m_0$ ³³, where m_0 is the bare electron mass 9.11×10^{-31} Kg. n is the carrier density, which is varying upon deflection of the piezoelectric cantilever. The additional carrier density is calculated by $\Delta n = Q(t)/(wLd_p)$, d_p denotes the depletion thickness on the surface of the piezoelectric, which can be approximated according to the Poisson equation $\frac{d^2\phi(z)}{dz^2} = \frac{e\Delta n}{\varepsilon_s}$. Here for simplicity it is taken as a constant 10 nm. $f_0(\mathcal{E})$ is the Fermi distribution of electrons $\frac{1}{\exp\left(\frac{\mathcal{E}-\mu}{k_B T}\right) + 1}$, where \mathcal{E} is the electron energy, μ stands for the chemical potential, k_B is the Boltzmann constant (8.62×10^{-5} eV/K⁻¹), and T denotes the temperature. Iteration method/self-consistent method is used to obtain μ through the numerical approach³⁴. In the work we calculate the Fermi distributions of electrons in conduction band f_e and holes in valence band f_h , where the electrochemical potentials μ_e and μ_h are electrochemical potentials for electrons and holes respectively. The effective mass of heavy hole is taken as $3.68m_0$ ³³. Focusing on the interface between QD and piezoelectric material, accumulated electrons due to piezoelectric effect causes electrochemical potential move to the conduction band minimum μ_c . Accumulated holes at the interface tend to shift the chemical potential to the valence band maximum μ_v . The middle of the bandgap g_b is set to potential 0, $\mu_c = g_b/2$, $\mu_v = -g_b/2$. To solve the equation (5), the integral is calculated from conduction band minimum to a large value of \mathcal{E}_m or from $-\mathcal{E}_m$ to the valence band maximum, $\mathcal{E}_m = 100 \times k_B T$ is large enough to arrive at an accurate result. Calculated chemical potential μ_e and μ_h are then mapped to the energy graph considering the bandgap g_b . For AlN, $g_b = 6.2$ eV³⁵. The mapped electrochemical potential has been designated as the chemical potential of the piezoelectric interface $\mu_p = [\mu_e + g_b/2, (n_e > n_h)] \cup [-\mu_h - g_b/2, (n_e < n_h)]$. Figure 1b schematically

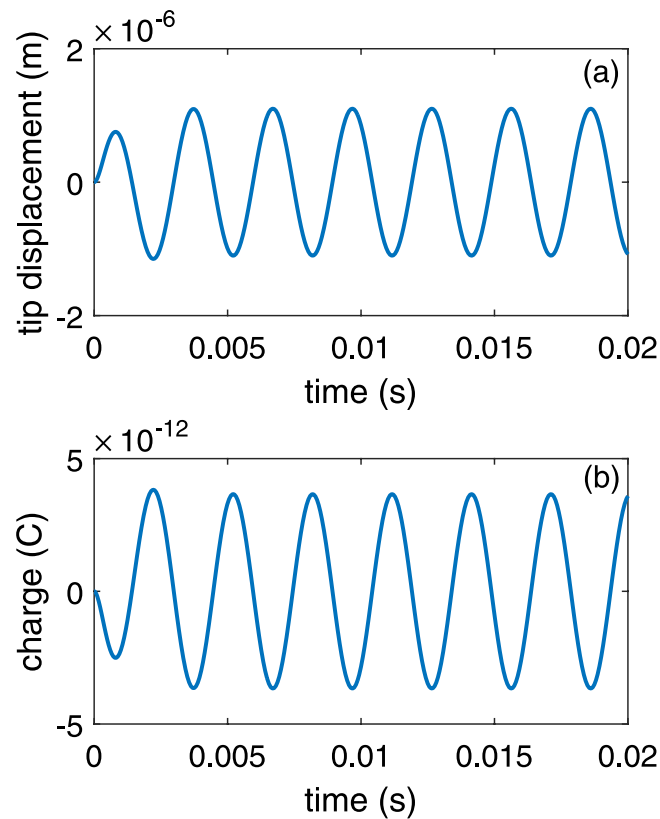


Figure 2. Vibration of the cantilever inducing electrical charges, frequency is calculated to be 335.9 Hz. (a) Tip deflection vs. time. (b) Generated charge vs. time t .

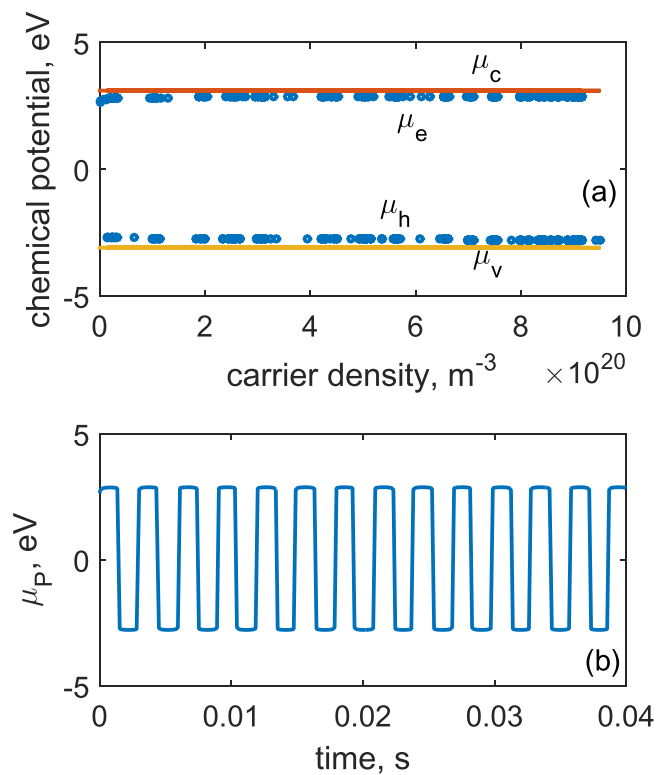


Figure 3. Chemical potentials calculated from the increase of carrier density and polarity change of generated charges on the piezoelectric surface due to vibration of the piezoelectric cantilever. (a) μ_e , μ_h , μ_c and μ_v in relation to the carrier density. (b) μ_p vs. time t .

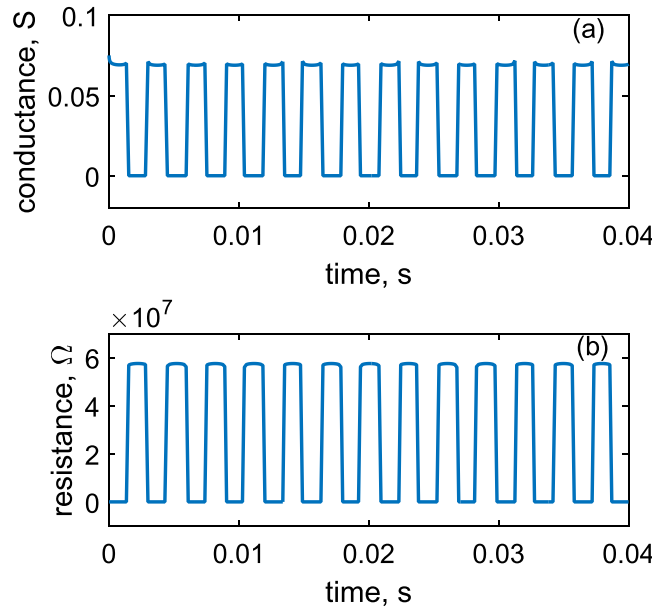


Figure 4. Calculated conductance and resistance of the QD layer with respect to time. (a) Conductance vs. t . (b) Resistance vs. t .

displays the energy graph of the metal-QD-piezoelectric material interface. It is assumed that the piezoelectric material is intrinsic with the initial chemical potential in the middle of the bandgap, i.e. internal screening³⁶ of piezoelectric polarization is minimal. This assumption is reasonable as the AlN films exhibit very low carrier concentration in the real case.

Elastic tunnelling. In the normal operation conditions of the integrated piezoelectric vibrational energy harvesting device, surrounding temperature is usually room temperature. The energy cost to add an electron to the dot is determined by the dot's self-capacitance, that is e^2/C_Σ . Simple estimation of the self-capacitance is $C_\Sigma = e^2/(8\varepsilon_r\varepsilon_0R)$ ³⁷ where R is the radius of a 2D dot. For a typical GaAs dot with radius of 50 nm, C_Σ is calculated to be 0.046 fF, resulting in $e^2/C_\Sigma = 3.5$ meV, much smaller than thermal energy at room temperature 300 K, $k_B T = 25.9$ meV. Hence Coulomb blockade effect can be ignored in this analysis. After μ_p is obtained, electrical current I flowing through the quantum dot is derived using the Landauer formula^{24,38}, that is

$$I = \frac{e}{h\pi} \int_{-\infty}^{\infty} \Gamma(\mathcal{E})(f_T - f_p)d\mathcal{E} \quad (6)$$

where f_T and f_p are electron Fermi distributions for the top electrode (note the QD layer is deposited on the top surface) and piezoelectric layer respectively, $f_T = f(\mathcal{E} - \mu_T, T) = \frac{1}{\exp((\mathcal{E} - \mu_T)/(k_B T)) + 1}$, $f_p = f(\mathcal{E} - \mu_p, T) = \frac{1}{\exp((\mathcal{E} - \mu_p)/(k_B T)) + 1}$. In the analysis, temperature T remains constant 300 K. Here we shall calculate the μ_p according to the previous section, and μ_T is assumed to be 0, aligning with the chemical potential of the initial state of the device. Without external mechanical excitation, the initial chemical potential of the piezoelectric layer μ_p^0 is 0. $\Gamma(\mathcal{E})$ represents the transmission function of the two interfaces for each incident electron energy \mathcal{E} . It is governed by the Lorentzian equation

$$\Gamma(\mathcal{E}) = \frac{\gamma_T \gamma_p}{(\mathcal{E} - \mathcal{E}_{qd})^2 + \left(\frac{\gamma_T + \gamma_p}{2}\right)^2} \quad (7)$$

where the γ_{Tp} represents the elastic tunnel coupling coefficients through electrode-quantum dot, and quantum dot-piezoelectric layer respectively. They are determined by $\gamma_0 \exp(-\delta z/\xi)$ ³⁹, here δz denotes the distance between quantum dot edge and the electrode, quantum dot edge and piezoelectric layer. ξ is the characteristic length of the dot defining the exponential decay for the probability of finding electron outside the dot, i.e. decay of the wavefunction of the electron, which can normally be calculated from theory of electron passing barriers. Here in this analysis it is assumed that $\gamma_0 = k_B T$. For the simulation we set $\delta z = 20$ nm, $\xi = 2$ nm, then we have $\gamma_{Tp} = 0.45 \times 10^{-4} k_B T$. It is worth noted that γ_{Tp} can be adjusted by changing positions of the QDs to achieve various rectification effects. The energy level of the quantum dot \mathcal{E}_{qd} is set to 1.1 eV (Here the fluctuation of the \mathcal{E}_{qd} due to electrons flowing through the dot is not considered). Here we design the in-plane spacing between dots to be much larger than ξ , so that the current flow between dots can be neglected. The conductance of the quantum dots layer is

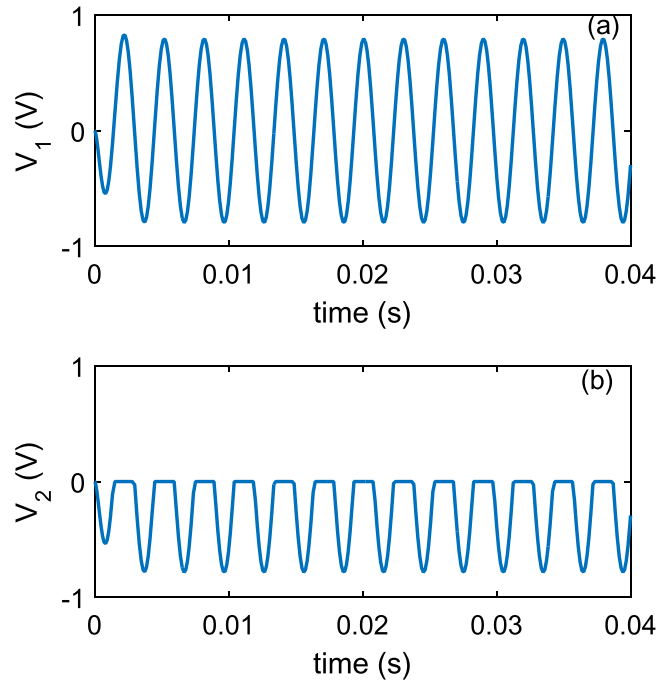


Figure 5. Simulation of the rectification effect of the integrated piezoelectric harvester. (a) Voltage with respect to the time for piezoelectric layer. (b) Voltage vs. t for the integrated device.

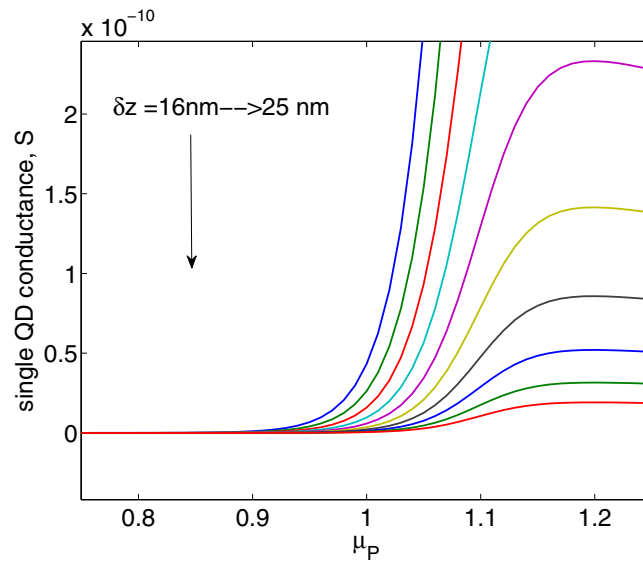


Figure 6. Conductance vs. chemical potential of piezoelectric layer.

$$G = \frac{I}{V_D} = \frac{eI}{\delta\mu} = \frac{e^2}{\hbar\pi\delta\mu} \int_{-\infty}^{\infty} \Gamma(\mathcal{E})(f_T - f_p)d\mathcal{E} \quad (8)$$

where the integral is calculated for the energy range of $(-200k_B T, 200k_B T)$, which is sufficient to cover the varying potential of the piezoelectric material. Once G is obtained, further analysis on the integrated harvester connecting with an external load is discussed. The complete circuit consists of a load resistor and the integrated QD-piezoelectric energy harvester (Fig. 1c). It is assumed that the piezoelectric material has infinite resistance i.e. a pure capacitor. As the cantilever is vibrating under the external load, conductance/resistance of the quantum dots layer changes with the varying μ_p , only allowing electrons having energy within a certain band passing through. The next section demonstrates numerical analysis of the integrated harvester.

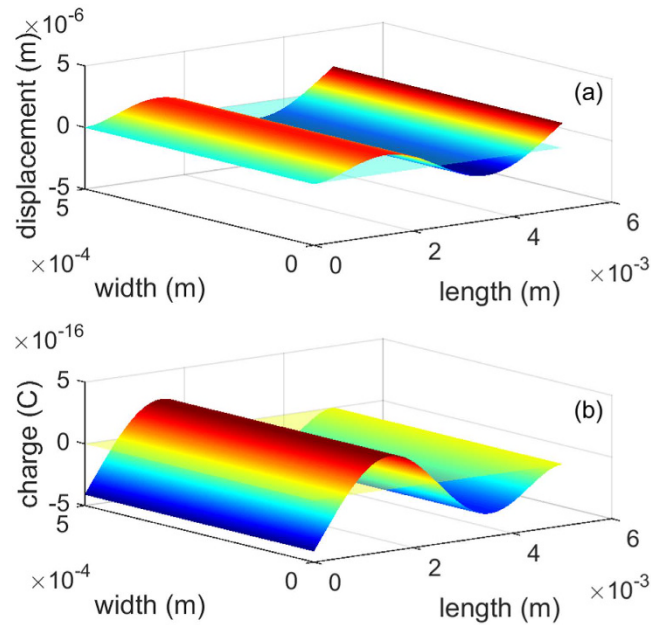


Figure 7. Third resonant mode shape of the cantilever and charge distribution. (a) 3D view of the mode shape. (b) Charge distribution. Without QDs layer, the net value of charges is -2.6×10^{-11} C. With QDs layer, the net value of charges is -5.8×10^{-11} C. Cantilever in static and charge in neutral are also shown in the figure (semi-transparent plane).

Results and Discussion

Mechanical analysis. A case study to quantitatively demonstrate this idea is detailed in this section. The numerical procedure begins with the mechanical analysis. In solving the equation (1), the amplitude of periodic driving force A is set to $m_t a$ where m_t is the sum of the cantilever mass and the proof mass, a denotes the externally applied acceleration (10 m/s^2). The linear stiffness of the cantilever can be calculated from $k_1 = (Ywg^3)/(4L^3)^{40}$, nonlinear stiffness $k_2 = 2k_1$, and the damping factor is usually very small for miniaturized devices. Here we use $b = 2(k_1/m_t)^{1/2} \times 10^{-5}$. From the numerical solution of the equation (1), substitute tip deflection $z(t)$ into the equations (2–4), generated charge $Q(t)$ is calculated with respect to time t . Figure 2 depicts the result of $z(t)$ and $Q(t)$. It is seen that the cantilever oscillates periodically with a maximum peak displacement of $1.1 \mu\text{m}$, generated charge oscillating in a similar manner with the peak amplitude of 3.66×10^{-12} C.

Chemical potential. Next the resulting charge values are input to the equation (5) to arrive at chemical potentials μ_c and μ_h , which are mapped to the band diagram and shown together with μ_c and μ_v in Fig. 3. It is seen from Fig. 3a that in the low density range, a small addition of the carrier density causes chemical potential to deviate to μ_c or μ_v rapidly. But the chemical potential remains steady in the large density range. That is due to the exponential nature of the Fermi-Dirac distribution of electrons in both conduction and valence bands. As the cantilever vibrates, the chemical potential on the top side of the piezoelectric layer (attaching to the QDs) μ_p with respect to time t is shown in the Fig. 3b. Compared with the results in Fig. 2b, μ_p curve displays a square wave instead of a sinusoidal, which coincides with the results of μ_c and μ_h versus carrier density.

Analysis of conductance. Further on, the electrochemical potential μ_p is used to calculate the equation (8) for the purpose of obtaining conductance as the function of time t . Conductance $G(t)$ is then obtained numerically for a single quantum dot. Suppose dots density is $2.78 \times 10^{14} \text{ m}^{-2}$, total conductance of the whole surface area of the cantilever G_t can be considered to be the sum of many single conductances G_0 connected in parallel. Then it is $G_t = \sum G_0 = 6.94 \times 10^8 G_0$. The results are shown in the Fig. 4, where both $R(t)$ (resistance) and conductance $G(t)$ curves are displayed. Conductance varies from a very low value ($1.74 \times 10^{-8} \text{ S}$) to a high value (0.07 S), corresponding to resistance from $5.74 \times 10^7 \Omega$ to 14.5Ω . A simple circuit consisting of the integrated device and a $1 \text{ k}\Omega$ resistor is sketched to demonstrate the rectification effect. From Fig. 5, clearly the rectification effect has been achieved and almost all positive part of the voltages has been blocked due to very large impedance of the QDs layer, attributed to its energy selection mechanism, where V_1 and V_2 refer to the equivalent circuit in Fig. 1c. Graphical demonstration of conductance vs. chemical potential ($G-\mu_p$) curve with the varying δz for a single QD is shown in Fig. 6, which clearly displays a performance similar to that of diodes. As the current flows through the close-loop circuit consisting of a finite external load resistance, the electrochemical potential μ_p shifts to the neutral. Results from equation (5) (Fig. 3b) reveals that the variation of the μ_p is mainly determined by the polarity of the accumulated charges in the QD-Piezoelectric interface. A small quantity of charges will bring the μ_p close to μ_c or μ_v , and further increasing the quantity does not vary μ_p significantly (Fig. 3a). This makes the metal-QD-piezoelectric interface as a perfect rectifier compared to the classic diodes that require a forward bias.

Complex mechanical vibration. Complex motions of the mechanical structure give charges with opposite signs on the the same surface, for example a 3rd resonant mode displayed in Fig. 7. The mode shape is obtained from Euler–Bernoulli beam theory on cantilever resonance⁴¹, the 3rd resonant mode is found by numerically solving the third root β_3 of the nonlinear equation $\cosh(\beta_n L)\cos(\beta_n L) + 1 = 0$. d^2z/dx^2 is for the curvature at x point of the cantilever. Subsequently the mode shape and charge distribution can be calculated. It is seen that both positive and negative charges are generated on the surface, causing charges cancellation. With the QDs layer, only one type of charges can flow through, reducing the current loss on electrode. Though this hypothesis is mainly based on the theoretical validation, experiments in previous published work⁴² on thermoelectric energy devices showed that using QDs in power generation devices is viable.

Conclusion

An integrated piezoelectric energy harvesting concept comprising a quantum dots layer and a piezoelectric layer stacked together is reported in this article. The new structure enables rectification function to be achieved without additional external circuits, as well as avoidance of the screening effect on the surface of the piezoelectric material. Multiphysical simulations taking account of the mechanical-electrical, charge-chemical potential, and elastic tunnelling process validate the concept. The modelling results show clearly that the rectification effect has been achieved. It is worth mentioning that this configuration can be applied to other structures besides the cantilever shape.

References

1. Beeby, S. P., Tudor, M. J. & White, N. M. Energy harvesting vibration sources for microsystems applications. *Measurement Science and Technology* **17**, R175–R195 (2006).
2. Jeon, Y., Sood, R., Jeong, J. & Kim, S. Mems power generator with transverse mode thin film pzt. *Sensors and Actuators A-Physical* **122**, 16–22 (2005).
3. Cook-Chennault, K. A., Thambi, N. & Sastry, A. M. Powering mems portable devices - a review of non-regenerative and regenerative power supply systems with special emphasis on piezoelectric energy harvesting systems. *Smart Materials and Structures* **17**, 043001 (2008).
4. Li, H. *et al.* An Energy Harvesting Underwater Acoustic Transmitter for Aquatic Animals. *Scientific Reports* **6**, 33804 (2016).
5. Wang, Z. L. & Song, J. H. Piezoelectric nanogenerators based on zinc oxide nanowire arrays. *Science* **312**, 242–246, doi: 10.1126/science.1124005 (2006).
6. Yang, Y. *et al.* Flexible hybrid energy cell for simultaneously harvesting thermal, mechanical, and solar energies. *ACS Nano* **7**, 785–790, doi: 10.1021/nn305247x (2013).
7. Li, H., Tian, C. & Deng, Z. D. Energy harvesting from low frequency applications using piezoelectric materials. *Applied Physics Reviews* **1**, 041301 (2014).
8. Ramadass, Y. K. & Chandrakasan, A. P. An efficient piezoelectric energy harvesting interface circuit using a bias-flip rectifier and shared inductor. *IEEE Journal of Solid-State Circuits* **45**, 189–204 (2010).
9. Ottman, G. K., Hofmann, H. F. & Lesieutre, G. A. Optimized piezoelectric energy harvesting circuit using step-down converter in discontinuous conduction mode. *IEEE Transactions on Power Electronics* **18**, 696–703 (2003).
10. Ottman, G. K., Hofmann, H. F., Bhatt, A. C. & Lesieutre, G. A. Adaptive piezoelectric energy harvesting circuit for wireless remote power supply. *IEEE Transactions on Power Electronics* **17**, 669–676 (2002).
11. Fang, H.-B. *et al.* Fabrication and performance of mems-based piezoelectric power generator for vibration energy harvesting. *Microelectronics Journal* **37**, 1280–1284 (2006).
12. Ferrari, M., Ferrari, V., Guizzetti, M., Marioli, D. & Taroni, A. Piezoelectric multifrequency energy converter for power harvesting in autonomous microsystems. *Sensors and Actuators A-Physical* **142**, 329–335 (2008).
13. Erturk, A. & Inman, D. J. An experimentally validated bimorph cantilever model for piezoelectric energy harvesting from base excitations. *Smart Materials and Structures* **18**, 025009 (2009).
14. Challa, V. R., Prasad, M. G., Shi, Y. & Fisher, F. T. A vibration energy harvesting device with bidirectional resonance frequency tunability. *Smart Materials and Structures* **17**, 015035 (2008).
15. Liu, H., Lee, C., Kobayashi, T., Tay, C. J. & Quan, C. Piezoelectric mems-based wideband energy harvesting systems using a frequency-up-conversion cantilever stopper. *Sensors and Actuators A-Physical* **186**, 242–248 (2012).
16. Wu, H., Tang, L., Yang, Y. & Soh, C. K. Development of a broadband nonlinear two-degree-of-freedom piezoelectric energy harvester. *Journal of Intelligent Material Systems and Structures* **25**, 1875–1889 (2014).
17. Chew, Z. & Li, L. Design and characterisation of a piezoelectric scavenging device with multiple resonant frequencies. *Sensors and Actuators A-Physical* **162**, 82–92 (2010).
18. Andosca, R. *et al.* Experimental and theoretical studies on mems piezoelectric vibrational energy harvesters with mass loading. *Sensors and Actuators A-Physical* **178**, 76–87 (2012).
19. Yu, H., Zhou, J., Yi, X., Wu, H. & Wang, W. A hybrid micro vibration energy harvester with power management circuit. *Microelectronics Engineering* **131**, 36–42 (2015).
20. Romani, A., Tartagni, M., Sangiorgi, E. & Paganelli, R. P. An energy autonomous switching converter for harvesting power from multiple piezoelectric transducers. In *2010 IEEE Sensors Conference, Kona, HI*, 1173–1176 (2010).
21. Mei, J. & Li, L. Split-electrode piezoelectric scavengers for harvesting energy from torsional motions. *Journal of Physics Conference Series* **476**, 012136 (2013).
22. Liu, Z. & Li, L. Modeling of energy harvesting device with segmented piezoelectric layer. In *26th European Conference on Solid-State Transducers, Eurosensors 2012 vol. 47*, 470–473 (2012).
23. Li, L. & Ronan, G. A. *Piezoelectric Energy Harvesting Device or Actuator*. PCT/GB2012/052741 (Patent, 2012).
24. Datta, S. *Quantum Transport: Atom to Transistor* (Cambridge University Press, Cambridge, UK, 2005).
25. Chen, Q., Qin, L. & Wang, Q.-M. Property characterization of aln thin films in composite resonator structure. *Journal of Applied Physics* **101**, 084103 (2007).
26. Hahnlein, B., Schaaf, P. & Pezoldt, J. Size effect of young's modulus in aln thin layers. *Journal of Applied Physics* **116**, 124306 (2014).
27. Jin, L., Mei, J. & Li, L. Analysis of intrinsic localised mode for a new energy harvesting cantilever array. *European Physical Journal - Applied Physics* **66**, 10902 (2014).
28. Moheimani, S. O. R. & Fleming, A. J. *Piezoelectric Transducers for Vibration Control and Damping* (Springer London, 2006).
29. Erturk, A. & Inman, D. J. *Piezoelectric Energy Harvesting* (John Wiley and Sons, Inc., West Sussex, UK, 2011).
30. Sinha, N. *et al.* Piezoelectric aluminum nitride nanoelectromechanical actuators. *Applied Physics Letters* **95**, 053106 (2009).
31. Levi, A. F. J. *Applied Quantum Mechanics* (Cambridge University Press, Cambridge, UK, 2006).
32. Sze, S. M. & Ng, K. K. *Physics of Semiconductor Devices* (John Wiley and Sons, Inc., Hoboken, New Jersey, 2007).

33. Suzuki, M., Uenoyama, T. & Yanase, A. First-principles calculations of effective-mass parameters of aln and gan. *Phys. Rev. B* **52**, 8132–8139 (1995).
34. Zhang, Y. & Li, L. Piezophototronic effect enhanced luminescence of zinc oxide nanowires. *Nano Energy* **22**, 533–538 (2016).
35. Dubois, M.-A. & Murali, P. Properties of aluminum nitride thin films for piezoelectric transducers and microwave filter applications. *Applied Physics Letters* **74**, 3032–3034 (1999).
36. Briscoe, J. *et al.* Nanostructured p-n junctions for kinetic-to-electrical energy conversion. *Advanced Energy Materials* **2**, 1261–1268 (2012).
37. Sohn, L. L., Kouwenhoven, L. P. & Schon, G. *Mesoscopic Electron Transport* (Series: Nato Science Series E, Vol. 345, 1997).
38. Jordan, A. N., Sothmann, B., Sánchez, R. & Büttiker, M. Powerful and efficient energy harvester with resonant-tunneling quantum dots. *Phys. Rev. B* **87**, 075312 (2013).
39. Li, L. & Jiang, J.-H. Staircase quantum dots configuration in nanowires for optimized thermoelectric power. *Scientific Reports* **6**, 31974 (2016).
40. Poggi, M. A., McFarland, A. W., Colton, J. S. & Bottomley, L. A. A method for calculating the spring constant of atomic force microscopy cantilevers with a nonrectangular cross section. *Analytical Chemistry* **77**, 1192–1195 (2005).
41. Gere, J. M. & Timoshenko, S. P. *Mechanics of Materials* (Brooks/Cole, 2003).
42. Thierschmann, H. *et al.* Three-terminal energy harvester with coupled quantum dots. *Nature Nanotechnology* **10**, 854–858, doi: 10.1038/NNANO.2015.176 (2015).

Acknowledgements

LL appreciates the support of college of engineering, Swansea University. This work was supported by the UK EPSRC (EP/H004742/1).

Additional Information

Competing Interests: The author declares no competing financial interests.

How to cite this article: Li, L. Rectifying the output of vibrational piezoelectric energy harvester using quantum dots. *Sci. Rep.* **7**, 44859; doi: 10.1038/srep44859 (2017).

Publisher's note: Springer Nature remains neutral with regard to jurisdictional claims in published maps and institutional affiliations.



This work is licensed under a Creative Commons Attribution 4.0 International License. The images or other third party material in this article are included in the article's Creative Commons license, unless indicated otherwise in the credit line; if the material is not included under the Creative Commons license, users will need to obtain permission from the license holder to reproduce the material. To view a copy of this license, visit <http://creativecommons.org/licenses/by/4.0/>

© The Author(s) 2017